


## Precision in DIY lightweight manipulator

Krzysztof Piechota<sup>1\*</sup>, Jan Odrobiński<sup>1</sup>, Adrian Zakrzewski<sup>1</sup> , Maciej Zwierzchowski<sup>1</sup> 

<sup>1</sup> Faculty of Mechanical Engineering, Wrocław University of Science and Technology, ul. Ignacego Łukasiewicza 5, 50-371, Wrocław, Poland

\* Corresponding author's e-mail: kpiechota2003@gmail.com

### ABSTRACT

This article presents a comparative analysis of the precision of two DIY 6DOF robotic manipulators: a current model and a newly developed construction. The objective of the study was to evaluate and quantify the positional accuracy and repeatability of both designs. Both manipulators are lightweight (under 13 kg) and designed to handle payloads of up to 5 kg, making them suitable for installation on a mobile rover platform. The systems are primarily intended for teleoperation. Precision was assessed through experimental measurements, reflecting realistic operating conditions. The study demonstrates measurable improvements in the new design's precision and provides a foundation for further development of manipulator systems for mobile, teleoperated platforms.

**Keywords:** DIY manipulator, robotic arm, precision analysis, lightweight manipulator, rover-mounted systems.

### INTRODUCTION

The development of lightweight robotic manipulators that combine high load capacity with precise control has seen significant advancement in recent years. This progress is largely driven by the growing deployment of mobile robotic platforms in demanding applications such as planetary exploration [1], search-and-rescue missions [2], and competitive robotics challenges [3]. These scenarios require manipulators that are not only compact and lightweight but also robust and accurate enough to perform complex tasks reliably in unstructured and often harsh environments. For instance, the authors describe a manipulator weighing less than 10 kg that is capable of handling a 2 kg payload. Although originally designed for space applications, its design characteristics align closely with the requirements defined for the Scorpio Infinity rover's manipulator. The manipulator employs harmonic gearboxes coupled with frameless BLDC motors, enabling a repeatable positioning accuracy of 0.12 mm. Joint positions are monitored using absolute magnetic encoders, and the structure incorporates a hollow-body design to further reduce weight [4, 5]. The use of harmonic

gearboxes combined with frameless BLDC motors appears to be a standard in the design of lightweight, high-performance manipulators [4, 6, 7]. Harmonic drives offer compactness, high reduction ratios, and near-zero backlash, making them ideal for robotic joints where precise motion is required. In more torque-demanding joints, cycloidal gearboxes are also gaining attention due to their robustness, efficiency, and backlash-free operation under load [8, 9]. The integration of compact and efficient gear-motor units is a key factor in enabling lightweight design without compromising load capacity or precision.

One of the most effective strategies for enhancing manipulator positioning precision is the reduction of inertial forces. Numerous studies demonstrate the use of finite element method (FEM)-based topology optimization to refine the geometry of structural components. This approach has proven effective in decreasing part mass by up to 40% while preserving structural stiffness, thereby contributing to both reduced inertia and improved dynamic performance [4, 10, 11]. Additive manufacturing technologies – especially selective laser sintering (SLS) and continuous fiber 3D printing – are often used in conjunction with

topology optimization, enabling complex geometries optimized for stiffness-to-weight ratio [10, 12, 13]. Numerical simulation is a vital tool in the design and optimization of 6-DOF robotic manipulators. Finite element method (FEM) analysis is widely used to evaluate structural stiffness and deformation under operational loads, ensuring that lightweight designs maintain necessary rigidity. Additionally, dynamic and kinematic simulations provide insights into joint behavior, actuator requirements, and error propagation, which are critical for accurate motion control. Integrating these simulation methods facilitates a comprehensive assessment of manipulator performance prior to physical prototyping, reducing development time and improving design reliability [14–18].

The positioning precision of industrial manipulators is commonly assessed experimentally by evaluating pose accuracy and pose repeatability. The ISO 9283:1998 standard outlines a set of performance characteristics for such measurements, including the conditions under which they should be conducted [19]. However, it does not mandate specific methods for obtaining the end-effector's position or establishing an accurate reference point. Common methods for gathering effectors position include digital indicators, laser interferometers, and laser trackers. Digital indicators are cost-effective and easy to use, making them suitable for lab environments. Laser interferometers offer high precision but are complex and limited to linear paths. Laser trackers are widely used in industry, though their repeatability may not be sufficient for medium-sized robots. ISO 9283:1998 defines one-directional measurement as repeatedly moving the robot to a target pose from the same direction and path, which helps isolate internal mechanical consistency. In contrast, multi-directional measurement involves approaching the same target pose from varied directions and paths, capturing the effects of different joint configurations on positioning [19–21].

## MATERIALS AND METHODS

### General concept

#### *The Scorpio rover*

The study focuses on the development of a new robotic manipulator designed for the *Scorpio Infinity* rover (Figure 1), created specifically for the Rover Challenge competition series. The

rover is a four-wheeled vehicle, fitting within a 1.2×1.2×1.2 meter cube and weighing 37 kg without a manipulator. It is capable of traversing off-road terrain and is equipped with a rocker suspension system (1) and custom 3D-printed TPU tires (2). It is fully remotely operated, with navigation and steering enabled through a network of cameras. Notably, the integration of the ZED2i stereovision camera (3) allows for point cloud generation, which supports autonomous navigation and manipulation tasks. The Scorpio rover serves as a modular platform that accommodates various task-specific tools, such as a drilling module or a Raman spectrometer. However, the most critical module is the robotic manipulator (4). Until now, the Scorpio rover series has utilized a manipulator designed in 2016 – referred to in this publication as the previous construction. This arm featured six degrees of freedom and incorporated a diverse set of gearboxes. However, the performance of this design was significantly limited by several mechanical shortcomings.

#### *The previous construction*

In the base joint, gear transmissions were used, which introduced considerable backlash. The first wrist joint employed a worm gear combined with a small DC motor, which proved unreliable and offered low maximum angular velocity – noticeably reducing the manipulator's movement speed. Two segments were constructed from carbon fiber tubes, which successfully reduced the overall mass while maintaining sufficient stiffness. Another major limitation of the previous design was encoder placement. Absolute encoders were not part of the original concept and were added post-construction. As a result, they were mounted indirectly via 1:1 transmission 3D-printed gears. This setup introduced backlash that negatively impacted the manipulator's precision. The control system relied on custom boards capable of reading encoder values and controlling the DC motors at each joint, theoretically allowing for closed-loop control. However, the hysteresis resulting from indirect encoder placement significantly complicated the implementation of accurate velocity and inverse kinematics control.

#### *The improved construction overview*

This publication presents a newly developed manipulator that directly addresses the limitations of the previous design. The goal is to improve

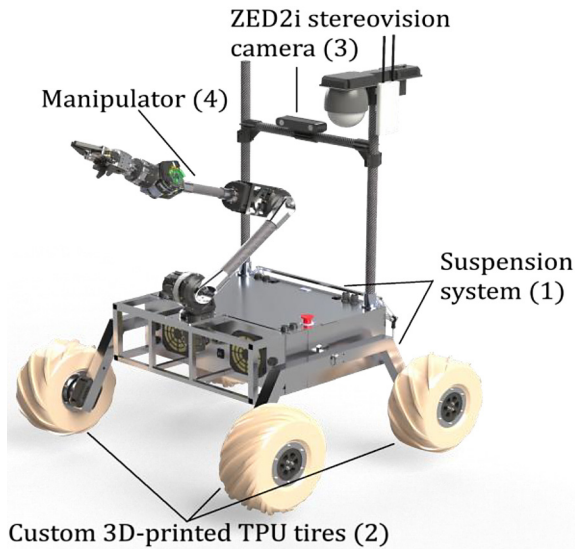


Figure 1. Manipulator on Scorpio infinity rover

precision, reliability, and dynamic performance to better support complex competition tasks and enable more effective autonomous manipulation. The primary objective is to create a high-precision robotic arm with six degrees of freedom (6DOF), tailored to meet the demanding requirements of these competitions. A schematic view of the developed lightweight manipulator is presented in Figure 2. To achieve this, a distinct set of design constraints were established. The most critical is a weight limit of 13 kilograms, dictated by the rover’s payload capacity. Despite this limitation, the manipulator must be capable of handling objects weighing up to 5 kilograms. To ensure the required precision, the structure was designed to be sufficiently stiff, with a maximum deformation

of less than 3 millimeters under full load. Minimizing backlash was a key design goal. Harmonic gearboxes were integrated into the first 4 joints - marked as (1) on Figure 2a, while custom cycloidal drives were implemented in the last two joints (2). This combination improves positioning accuracy and load-handling capacity. Compatibility with inverse kinematics was also prioritized to enable precise trajectory control, supported by absolute encoders for accurate joint position and speed feedback. Furthermore, slip rings (3) were used in the joint design to allow continuous rotation while avoiding cable twisting. For safety and reliability, the arm is capable of supporting its own weight plus a full 5-kilogram payload in the event of power loss. This new design builds upon earlier generations of Scorpio Infinity rover manipulators, addressing their key limitations – primarily poor positioning accuracy – and resulting in a significantly improved and competition-ready system. The critical issues of the manipulator are joint drivers, slip rings, carbon fibre material (4), as well as communication and control.

*The construction of joints and links*

In order to maximize precision a lot of effort was put in minimizing backlash. On Figure 3. Exploded view of joint A is shown. Harmonic gearboxes (3) were the first choice due to negligible backlash and good strength to weight ratio. It was decided to use an initial planetary gearbox (2) made out of polyamide parts created with additive manufacturing methods in base, shoulder and elbow joints. This way the target torque was

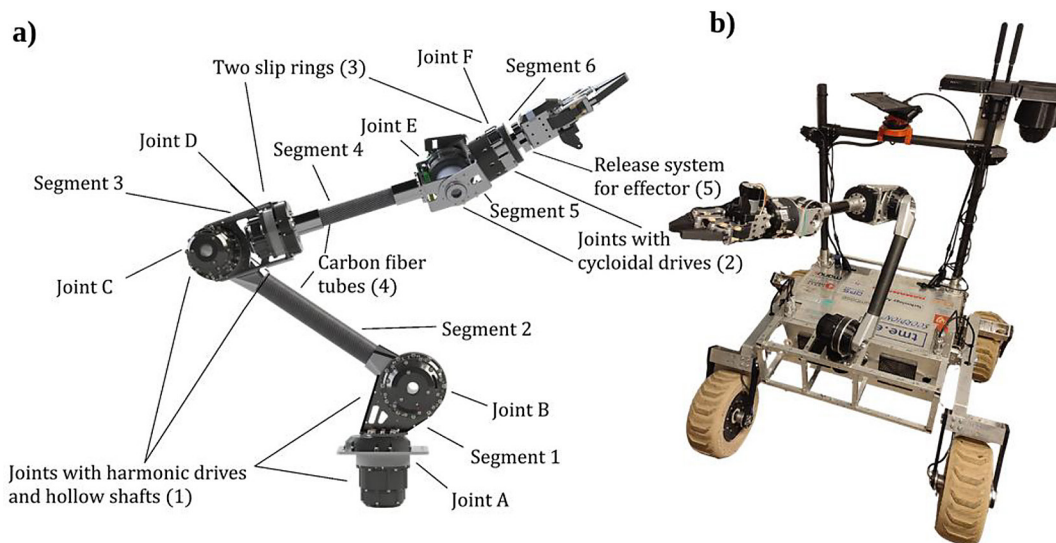


Figure 2. (a) Side view of the manipulator, (b) photo of the rover with the manipulator

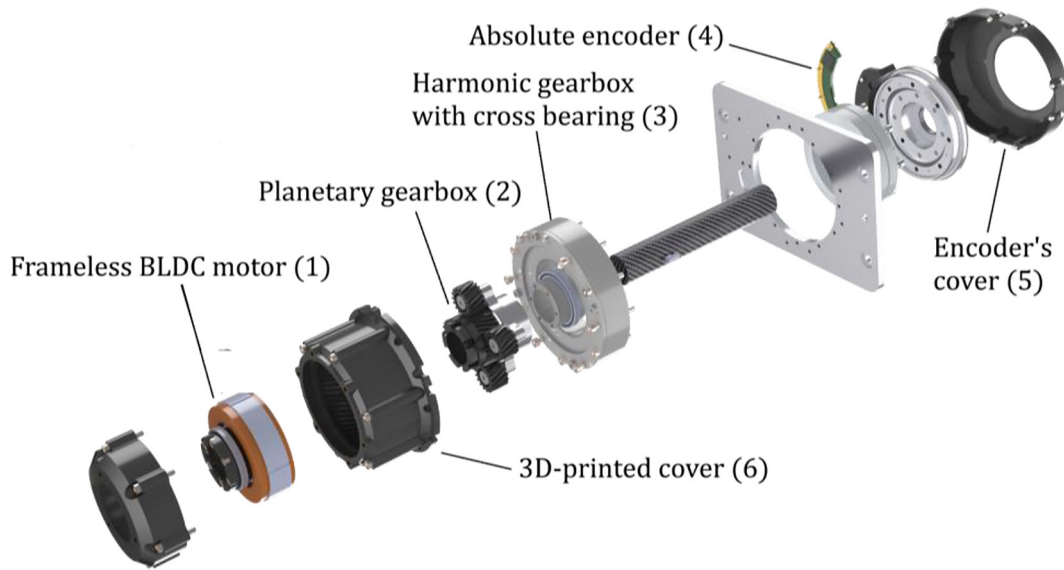


Figure 3. Exploded view of base joint

achieved as well as assumed maximum rotation speed of 5 RPM while minimizing weight.

As shown in Figure 4, custom cycloidal drives (4) were used in the last two joints. This design choice was aimed to reduce weight placed far from the base of the manipulator. Using aluminum 7075 as main material enabled creation of a gearbox weighing less than 200 grams.

All drives except the joint E (Figure 2) have hollow shafts which allow passing cables in a safe and convenient way. Frameless BLDC motors were used both to make hollow shafts possible and to reduce weight. Hollow shaft absolute encoders mounted directly on the output of gearboxes ensures precise 18-bit position reading.

To minimize constraints of movement slip rings were implemented in both wrist joints. The gold brush contact type was chosen due to its small size and electrical noise small enough to pass CAN bus and Ethernet through both wrists. The design of the manipulator uses two carbon tubes for connecting joints. This solution enables possibility to achieve good stiffness while remaining light weight and slim shape which is important to interrupt view from cameras as little as possible. Carbon tubes are glued in aluminum to create strong and durable bolt connections. Using carbon fiber tubes is a solution tested in previous construction and achieved satisfactory performance. Use of carbon fiber laminates is limited

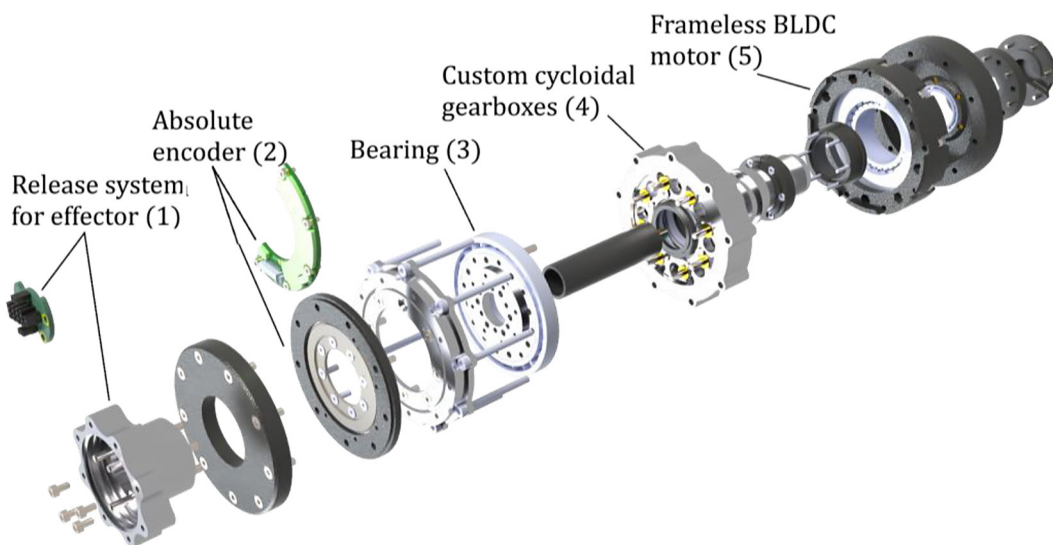


Figure 4. Exploded view of second wrist joint

to two tubes due to its anisotropic properties which make it difficult to design parts resistant to high loads in many directions.

### The control system

Each joint of the manipulator is equipped with a custom-designed STM32-based control board. These boards interface directly with 18-bit absolute encoders and dedicated BLDC motor drivers, and communicate with the central control unit via a CAN bus. Joint positions are sampled at 300 Hz. The control boards estimate the actual joint velocities in real time by applying a moving average filter to consecutive encoder readings, which significantly improves the stability and accuracy of the velocity signal by reducing noise and short-term fluctuations. These measurements are used within PID controllers, supporting three control modes: power, velocity, and position. In typical operation, the system runs in velocity control mode. Regardless of the chosen mode, the control boards output motor power commands to the drivers. The drivers, using feedback from embedded Hall-effect sensors, ensure stable and accurate commutation of the BLDC motors. Desired joint velocities are computed on the central computer by an inverse kinematics-based trajectory tracking module. Rather than solving inverse kinematics statically for a target pose, this module continuously converts a desired end-effector trajectory into a time-parameterized sequence of joint velocity setpoints. This ensures that the manipulator follows the trajectory smoothly. The module is implemented within the ROS 2 framework and builds upon the MoveIt2 motion planning library. Trajectories are defined and managed via a custom web-based interface used to operate the rover.

## Determination of critical elements of the manipulator

### The length of the segments

The length of the manipulator's segments plays a crucial role in the precision of its positioning. Even minimal angular deviations in the joints lead to positioning errors that are proportional to the length of the segments. Furthermore, extending the manipulator's elements increases their tendency to deflect under applied loads. For this reason, it is essential to carefully select the length of the segments to ensure the required working range

while minimizing the risk of losing precision due to excessive elongation of the components.

For the selected manipulator kinematics, due to the relative positioning of the individual rotational pairs, the lengths of segment 2 (according to notation shown in Figure 2A) and the sums of the lengths of segments 3 and 4, as well as segments 5 and 6, are crucial for the accuracy of the manipulator's positioning. According to the assumptions, the maximum working range of the manipulator has been set at 1200 mm. Additionally, due to the design of the end effector and the need to provide sufficient space for the joints E and F, the total length segments 5 and 6 has been defined as 320 mm. It was also assumed that the length of segment 3 should be as small as possible, allowing the drive to be placed closer to the base of the manipulator, thus reducing the loads. Furthermore, the mounting place of the manipulator to the rover's frame causes the possibility of collision between segment 2 and the frame in certain configurations. To prevent this, the axis of rotation of joint B was offset by 50 mm from the axis of rotation of joint A. Based on these constraints, the total length of segments 2, 3 and 4 is 830 mm.

To determine the lengths of the segments, a graphical method was used by plotting the working area sections for four combinations of the considered segment lengths, which is shown in Figure 5. The following lengths were considered:

- $l_2 = 455$  mm;  $l_3 + l_4 = 375$  mm (green area),
- $l_2 = 375$  mm;  $l_3 + l_4 = 455$  mm (yellow area),
- $l_2 = 405$  mm ;  $l_3 + l_4 = 425$  mm (red area),
- $l_2 = 435$  mm;  $l_3 + l_4 = 395$  mm (blue area).

The manipulator should reach the front side of the rover's frame to operate various modules, so the combination of the segment's lengths that determine the working field of a yellow color was excluded from consideration. Among remaining configurations, the combination that provides the biggest reach in front and beneath the rover was selected, marked with red color. Based on this, the following segment lengths were determined:

- length of segment 2: 405 mm,
- the combined length of segments 3 and 4: 425 mm.

### The torques in the joint drives

Determining the torques required to move the manipulator joints is a key step in selecting the components of the drive system. Incorrect calculation of the required torques can lead to failure

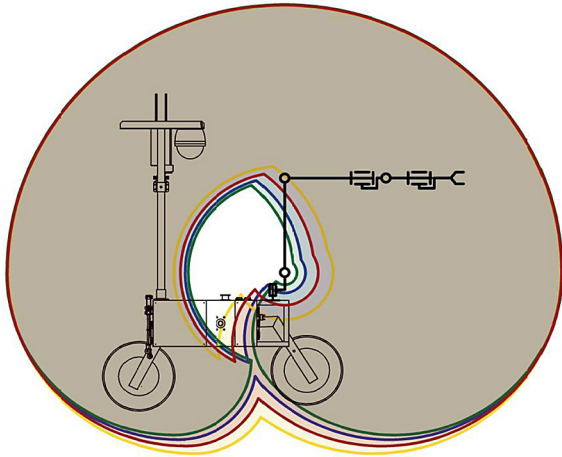


**Figure 5.** Cross-sections of the manipulator working area for the considered length combinations of segments 2, 3 and 4

to meet the manipulator’s load capacity parameters or, conversely, to the overdimensioning of the structure. This results in an increased weight, which may cause greater deflections of the manipulator’s segments.

To determine the required torques in joints B, C, and E, a load diagram was plotted for the manipulator at full extension, shown in Figure 6. Based on the initial assumed maximum weight of the manipulator, which is 13 kg, preliminary maximum drive masses were estimated in the individual joints. These masses were treated in the diagram as point forces acting on the system. Additionally, a continuous force was applied to the system, simulating the masses of the manipulator’s segments and equipment. A force of 50 N was applied to the end effector, taking into account the assumed load capacity of the manipulator. Assuming the system is in equilibrium, the required drive torques in the joints B, C and E were determined:

- $T_B = 106.9 \text{ Nm}$ ,
- $T_C = 53.6 \text{ Nm}$ ,
- $T_E = 17.3 \text{ Nm}$ .

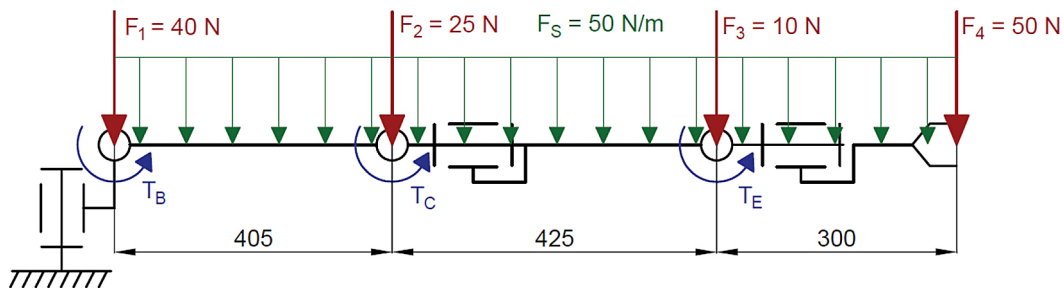


**Figure 6.** Scheme of loads acting on the manipulator

The torque required in joint A was determined by considering the operating conditions of the manipulator. The manipulator is mounted on a movable platform that operates under normal conditions with a tilt of up to 30°. It was assumed that the drive for joint A should generate an adequate torque to allow the movement of the manipulator with 5 kg load at full extension under this tilt. Given these assumptions, required torque in joint A equals 64.3 Nm.

The maximum torque acting on joint D occurs when the axis of motion of joint F is horizontal and perpendicular to the axis of rotation of joint D. Taking into account the moment resulting from the manipulator’s mass and the assumed load capacity, the required torque in joint D was determined to be 20 Nm.

The torque required in joint F is not dependent on the mass of the manipulator or the required load capacity. In this case, the tasks assigned to the manipulator were analyzed, and the required torque in joint F was determined to be 10 Nm.

#### Topology optimization by FEM

The FEM analysis allows for the verification of whether the designed components meet the strength requirements and for analyzing the displacements occurring in the elements under load. Due to the remote control of the manipulator and the potential errors that may arise, increasing the loads, the safety factor was set to 3.

The conducted analyses allowed for the optimization of the components both in terms of mass, which contributes to reducing the loads acting on the manipulator, and in terms of displacements, which increases the rigidity of the structure. Results of example analysis are shown in Figure 7.

Topology optimization is one of the FEM analysis methods that allows for precise identification of areas in the analyzed component where material can be removed without causing

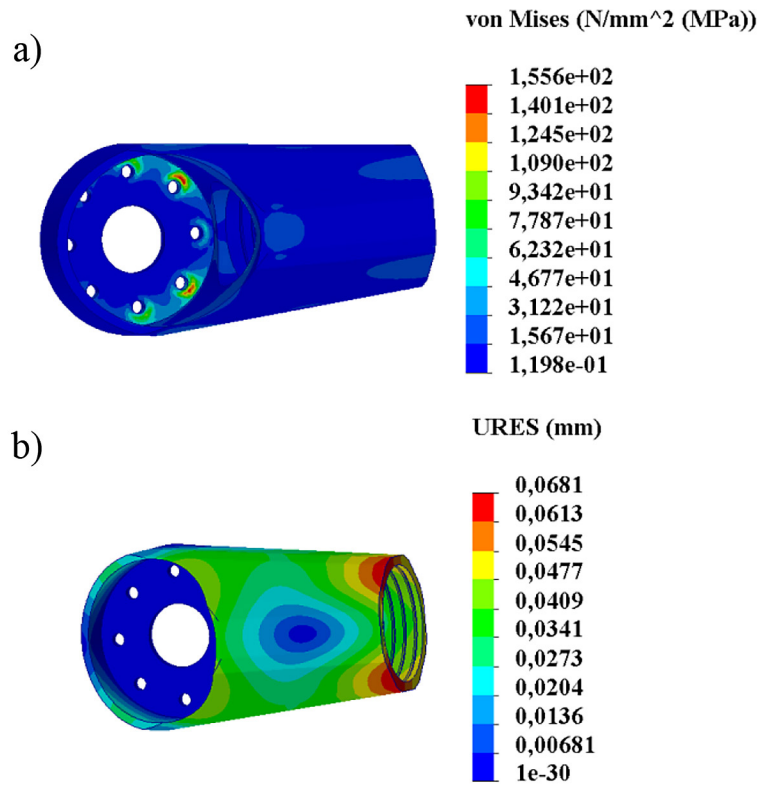


Figure 7. Example results of the FEM analysis for an element used in segment 2: (a) stress, (b) displacement

a significant loss in the stiffness or strength of the element. The analysis was performed on preliminarily designed components, whose adequate strength and stiffness were confirmed through FEM strength analyses in the SolidWorks Simulation module. After conducting the analyses, material was removed from the appropriate areas, enabling mass reduction. Following the topology optimization, the components were subjected to reanalysis for validation of the obtained results. Process of element's topology optimization is shown on Figure 8.

#### The segments cross-sections

As main elements for the longest segments, 2 and 4, carbon fiber composite tubes were used. To select the optimal cross-section, a review of the available tube cross-sections on the market was conducted. After an initial selection, cross-sections

that did not meet the strength requirements were discarded, and the maximum outer diameters of the tubes were determined, resulting from the need to reduce the size of the mounting components. For segment 2, the outer diameter was set at 40 mm, and for segment 3, at 30 mm.

The key criteria for selecting the components were determined to be the bending stiffness and the mass of the tubes, which result from the cross-sectional dimensions. For each considered cross-section, the bending stiffness, mass per linear meter, and the ratio of bending stiffness to mass were calculated (Table 1).

Based on the obtained results, the main element in segment 2 was selected as a tube with a 40 × 36 mm cross-section, which has the highest ratio of bending stiffness to mass. In the case of segment 4, tubes with 30 × 26 mm and 30 × 24 mm cross-sections were considered. The length

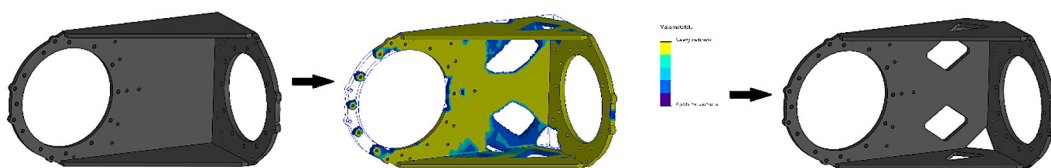


Figure 8. Scheme of component's topology optimization process

**Table 1.** Comparison of mass, stiffness and stiffness to mass ratio for the compared tubes cross-sections

| Outer diameter [mm] | Inner diameter [mm] | Mass [g/lm] | Bending stiffness [N·m <sup>2</sup> ] | Stiffness to mass ratio |
|---------------------|---------------------|-------------|---------------------------------------|-------------------------|
| 22                  | 18                  | 199         | 6346.02                               | 31.89                   |
| 26                  | 20                  | 342         | 14577.78                              | 42.63                   |
| 26                  | 22                  | 238         | 10932.74                              | 45.94                   |
| 30                  | 24                  | 402         | 23474.77                              | 58.39                   |
| 30                  | 26                  | 278         | 17329.03                              | 62.33                   |
| 32                  | 28                  | 298         | 21300.00                              | 71.48                   |
| 35                  | 31                  | 327         | 28328.53                              | 86.63                   |
| 37                  | 32                  | 428         | 40525.81                              | 94.69                   |
| 38                  | 34                  | 357         | 36756.63                              | 102.96                  |
| 38                  | 35                  | 272         | 28692.12                              | 105.49                  |
| 40                  | 30                  | 869         | 85902.92                              | 98.85                   |
| 40                  | 36                  | 377         | 43215.75                              | 114.63                  |

of the tube used in this arm is approximately 230 mm, which results in a mass difference of about 28.5 g in favor of the tube with the smaller wall thickness. However, the bending stiffness of this tube is approximately 25% lower. Due to the negligible mass difference, the tube with a 30×24 mm cross-section was chosen.

## RESULTS AND DISCUSSION

### Numerical analysis

During the manipulator design process, two key factors influencing effector’s positioning precision were analyzed: displacement of the effector’s working point from desired position caused by deflections of the manipulator’s segments, and additional displacement due to positioning errors of the joints. These factors were included in numerical calculations. Two cases were analyzed: the first - a manipulator at full reach, and the second - joints D and E are rotated 90° relative to full reach position, both under no-load conditions (Figure 9). The most pessimistic scenarios were considered, where positioning errors in the individual joints lead to a displacement of the working point in the direction of gravitational force. In the first case, the overall displacement of the working point is the cumulative effect of the inaccuracies in the positioning of joints A, B, C, and E, along with the deflection of the links caused by the manipulator’s own weight. In this configuration, the expected deflection of the effector’s working point should be maximal, but the influence of the positioning error in joint D is minimal. Therefore

the second case was analyzed, in which the influence of the joint D positioning inaccuracy for the manipulator’s positioning trueness is maximal. Analyses were conducted for both the new, improved manipulator and the previously used one. This approach provides a better assessment of the potential positioning precision improvement.

### Deflection of manipulator segments

The deflection of the manipulator segments was determined through FEM analysis performed using the SolidWorks Simulation module. At first, simplified 3D models of the constructions were created, from which finite element models were

Case 1:

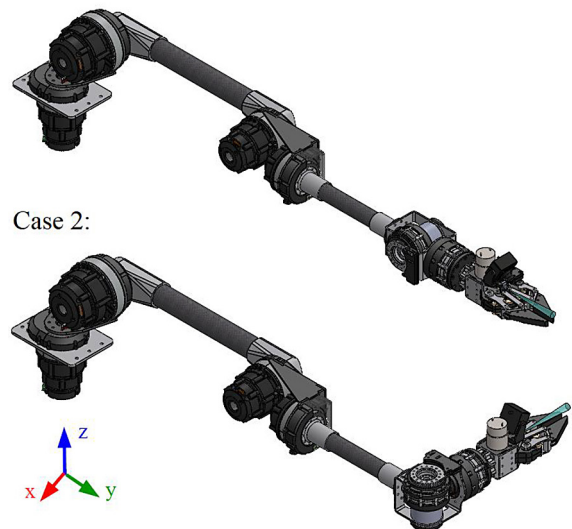


**Figure 9.** Two analyzed configurations of the manipulator with the indication of the applied coordinate system



made. Manipulators were fixed at the mounting spots, and a gravity load was applied. As the simplified models do not contain all the components, their weight was simulated as additional loads. Example of finished model, for first analyzed case of improved manipulator, is shown in Figure 10.

By performing the analysis, the deflection of the effector's working point in each axis was determined. The example results are shown in Figure 11, while Table 2 collects all the displacement values of the effector working point from the ideal position in each axis.

*The influence of the joints positioning error on the effector working point positioning trueness*

The positioning error of the joint is dependent on the accuracy of motor control, drive transmission and position reading by the encoder. It can be determined based on the relevant formula (1). Table 3 presents the maximum positioning errors for manipulator's joints. The positioning error of joint F is also included in the table, although due

to the kinematics of the manipulators in discussion, its position does not affect the position of the effector.

$$\Delta_l = \delta_m \cdot i_1 \cdot i_2 + \delta_{g1} \cdot i_2 + \delta_{g2} + \delta_e \quad (1)$$

where:  $\delta_m$  – motor positioning error,  $i_1$  – initial gearbox ratio,  $i_2$  – main gearbox ratio,  $\delta_{g1}$  – initial gearbox positioning error,  $\delta_{g2}$  – main gearbox positioning error,  $\delta_e$  – encoder positioning error.

To determine the effector's working point displacement influenced by joints position errors, a calculation models in Adams software were created. Then, in every joint, a movement was applied from the ideal position to a position with maximum error, according to the previously defined directions. The displacement of the effector was measured in each axis. Figure 12 presents the computational model with the adopted coordinate system.

Figure 13 shows example results of the simulations, for the first case and the improved

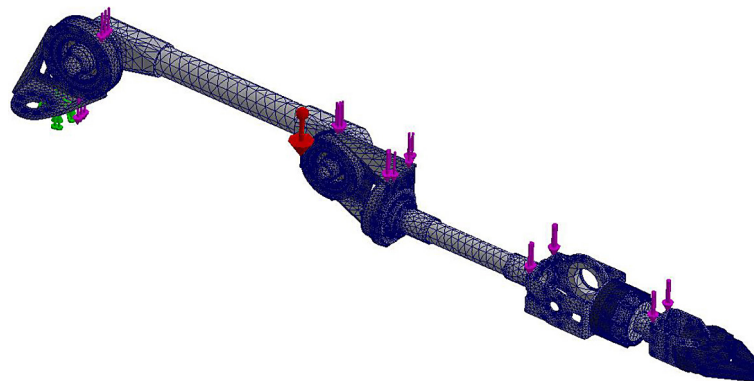


Figure 10. Example of FEM calculation model

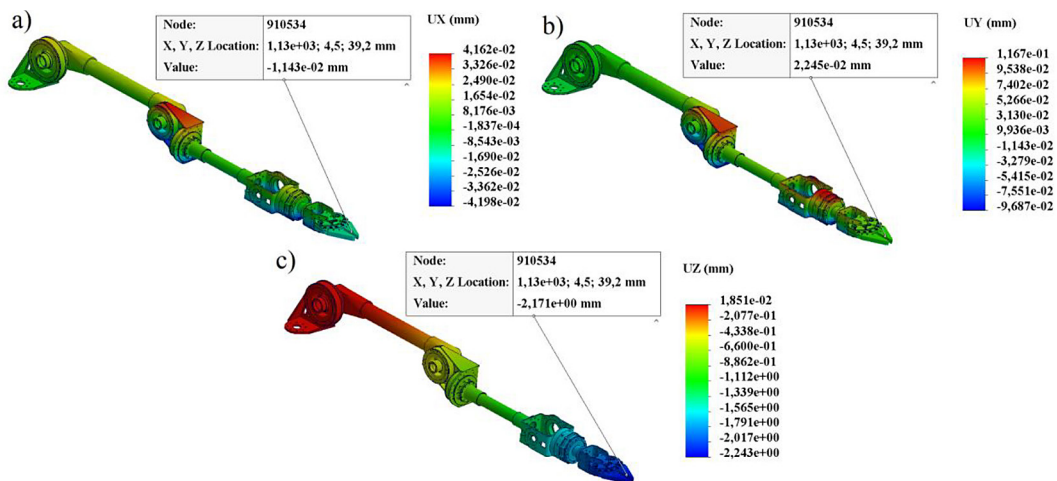


Figure 11. Results of the FEM analyses of one example case, deflection: (a) X-axis, (b) Y-axis, (c) Z-axis

**Table 2.** Displacement of the effector’s working point in each axis for each analyzed case, caused by segments deflection

| Displacement [mm] |                      |        |                      |        |
|-------------------|----------------------|--------|----------------------|--------|
| Axis              | Improved manipulator |        | Previous manipulator |        |
|                   | Case 1               | Case 2 | Case 1               | Case 2 |
| X                 | -0.01                | -0.03  | -0.18                | 0.13   |
| Y                 | 0.02                 | 0.01   | -1.25                | -0.97  |
| Z                 | -2.17                | -1.31  | -8.88                | -6.05  |

**Table 3.** Summary of maximum positioning errors of the joints

| Joint | Positioning error of the joint [°] |                      |
|-------|------------------------------------|----------------------|
|       | Improved manipulator               | Previous manipulator |
| A     | 0.085                              | 0.937                |
| B     | 0.085                              | 0.532                |
| C     | 0.085                              | 0.532                |
| D     | 0.109                              | 1.026                |
| E     | 0.264                              | 0.763                |
| F     | 0.393                              | 1.002                |

manipulator. The graph shows the displacement of the effector’s working point in each axis from the desired position to the resulting position, determined by the maximum positioning errors of the manipulator joints. Due to configuration of the manipulator in the analyzed case, the greatest displacement occurs in the vertical Z axis, while the smallest is observed in Y axis, aligned with the manipulator’s structure. Displacement results for all analyzed cases are shown in Table 4.

To fully evaluate and compare factors that affect positioning precision of the analyzed manipulators, displacements of the manipulator’s working point in each axis, caused by segments deflection and joints positioning errors, were

summed. Then, a total displacement was determined. The results are included in Table 5. The results of the numerical analyses show potential significant improvement in effector’s positioning precision. Accounting considered factors into the design process reduced displacement of the effector working point from ideal position, caused by segments deflection and joint positioning errors, by more than five times in both analyzed cases

**Experimental verification**

To evaluate manipulator positioning precision it was decided to experimentally obtain estimates for one-directional pose accuracy and repeatability. Chosen method is based on requirements listed in ISO 9283:1998 norm as its common use allows comparison with other studies. It was assumed that precision of a manipulator is a sum of pose accuracy and pose repeatability. Position data has been gathered from 4 points (P1, P2, P3, P4) in an imaginary cube (Figure 14). Position of the cube is set to measure precision characteristics in the area that is used the most. Location of point P0 in relation to the rover coordinate system is X = 700 mm, Y = 0 mm, Z = 365 mm, where the origin is in the center of the rover’s chassis. The edge of the cube is 250 mm, measurement points are

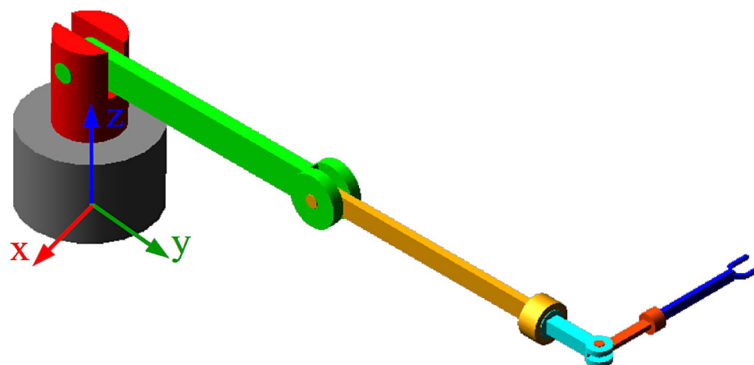


**Figure 12.** A model created in Adams software

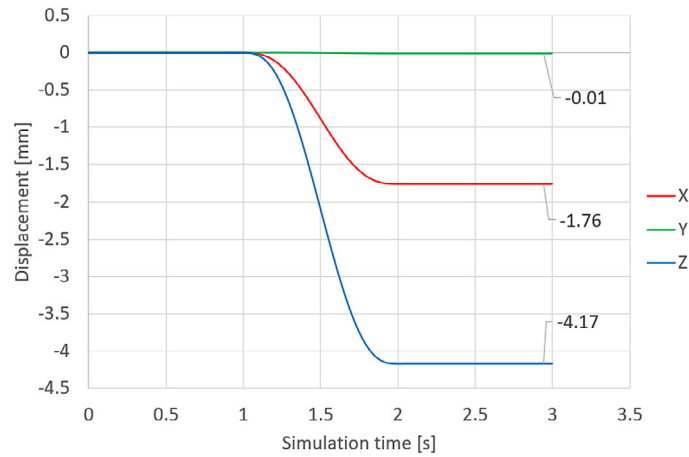


Figure 13. Simulation results of the first analyzed case, improved manipulator

Table 4. Displacement of the effector’s working point in each axis for each analyzed case, caused by joints positioning errors

| Displacement [mm] |                      |        |                      |        |
|-------------------|----------------------|--------|----------------------|--------|
| Axis              | Improved manipulator |        | Previous manipulator |        |
|                   | Case 1               | Case 2 | Case 1               | Case 2 |
| X                 | -1.76                | -1.30  | -19.80               | -15.16 |
| Y                 | -0.01                | -1.86  | -0.41                | -1.19  |
| Z                 | -4.17                | -2.44  | -22.36               | -18.45 |

Table 5. Displacement of the effector’s working point in each axis for each analyzed case, summed up

| Displacement [mm] |                      |        |                      |        |
|-------------------|----------------------|--------|----------------------|--------|
| Axis              | Improved manipulator |        | Previous manipulator |        |
|                   | Case 1               | Case 2 | Case 1               | Case 2 |
| X                 | -1.77                | -1.33  | -19.98               | -15.03 |
| Y                 | 0.01                 | -1.85  | -1.66                | -2.16  |
| Z                 | -6.34                | -3.75  | -31.24               | -24.50 |
| Total             | 6.85                 | 4.39   | 37.12                | 28.82  |

equally spaced out on the cube diagonal. Precise evaluation of origin position proved to be difficult, the method used is based on measuring distances from small cube in effector to 3 marked points on the rover. Based on the known positions of specific points on the rover, the position of the effector was calculated in the rover’s coordinate frame. Due to the limited precision of the used rangefinder (resolution of 1 mm) the method can have significant error of about 2 mm. Future iterations could benefit from high-precision optical tracking systems, which offer sub-millimeter accuracy and improved repeatability, enhancing the reliability of the results. Position measurements were taken at points P1... P4, position of each

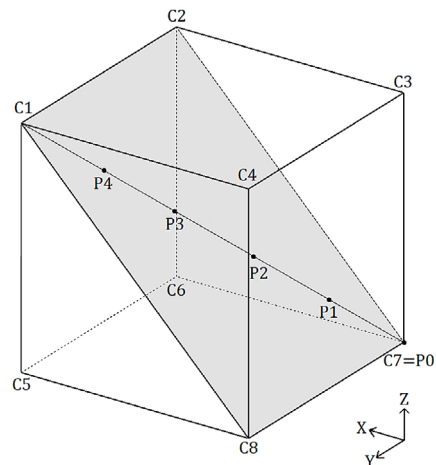


Figure 14. Imaginary cube with plane used for pose testing

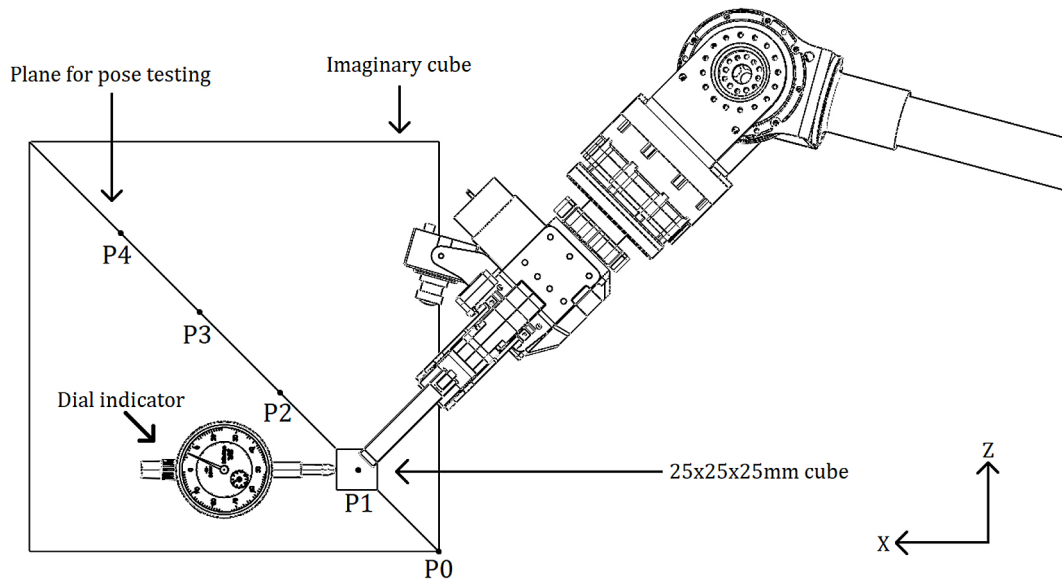


Figure 15. Measurement setup

point can be seen on Figure 15. For measuring in point P1 the end effector moved in path P0->P1->P0, stopping in position P1 for measurement as suggested in ISO 9283:1998 norm. Other points were treated the same way moving in path P(i-1)->Pi->P(i-1). Velocity during the test was set to 25% of maximum allowed by the control system - about 15 mm/s. Measurements were taken after stabilization of the manipulator using an analogue indicator with resolution of 0.01 mm. During tests a 25 × 25 × 25 mm cube was placed in the effector with an additional weight of 0.5 kg which is 10% of rated load. Test setup is shown on Figure 15.

The indicator can measure distance in only one direction, therefore 3 independent test series were conducted for each axis. Each series consisted of 20 cycles. The same set of measurements were repeated for the old manipulator construction. Results of one-directional pose repeatability can be seen in Table 6. Data suggests that previous construction of manipulator have values 2.4 times higher. In Table 7 the pose accuracy is presented. The obtained data shows that improved manipulator has better accuracy performance.

In this study, positioning precision is assumed to correspond to pose accuracy, while pose

Table 6. Summary calculated pose repeatability

| Point of measurement | Pose Repeatability [mm] |                      |
|----------------------|-------------------------|----------------------|
|                      | Improved manipulator    | Previous manipulator |
| P1                   | 3.828                   | 12.611               |
| P2                   | 4.997                   | 9.126                |
| P3                   | 3.486                   | 7.912                |
| P4                   | 3.760                   | 9.297                |

Table 8. Summary calculated positioning precision

| Point of measurement | Positioning precision [mm] |                      |
|----------------------|----------------------------|----------------------|
|                      | Improved manipulator       | Previous manipulator |
| P1                   | 9.063 ± 3.828              | 14.499 ± 12.611      |
| P2                   | 10.111 ± 4.997             | 15.502 ± 9.126       |
| P3                   | 6.728 ± 3.486              | 21.402 ± 7.912       |
| P4                   | 2.949 ± 3.760              | 14.276 ± 9.297       |

Table 7. Summary calculated pose accuracy

| Point of measurement | Pose Accuracy [mm]   |        |        |        |                      |        |        |        |
|----------------------|----------------------|--------|--------|--------|----------------------|--------|--------|--------|
|                      | Improved manipulator |        |        |        | Previous manipulator |        |        |        |
|                      | X                    | Y      | Z      | Total  | X                    | Y      | Z      | Total  |
| P1                   | 7.357                | 4.512  | -2.767 | 9.063  | 4.726                | -4.385 | 12.987 | 14.499 |
| P2                   | 3.359                | -2.844 | -9.103 | 10.111 | 13.519               | -3.325 | 6.819  | 15.502 |
| P3                   | -0.374               | 2.481  | 6.242  | 6.728  | 9.034                | -2.736 | 19.209 | 21.402 |
| P4                   | 1.974                | 0.196  | 2.183  | 2.949  | 9.682                | -7.697 | 7.130  | 14.276 |

**Table 9.** Comparison of positioning precision of chosen manipulators

| Manipulator                     | Declared positioning precision [mm] |
|---------------------------------|-------------------------------------|
| Previous manipulator (DIY)      | 21.402 ± 7.912                      |
| Improved manipulator (DIY)      | 10.111 ± 4.997                      |
| Light space manipulator [4]     | 0.12 (PR)                           |
| LR mate 200iC (FANUC) [22]      | 0.02 (PR)                           |
| 6-DOF robotic manipulators [14] | 0.01 (PR)                           |

repeatability is treated as the error associated with that value. The results are presented in Table 8.

Table 9 presents a comparison of positioning precision. The data should be treated as indicative only, as a direct comparison is difficult due to differing methods used to assess precision. The intention is to provide contextual reference, even though the manipulators serve different purposes. If the positioning precision is given in multiple points, the worst case is presented. Some manipulators have only pose repeatability (PR) measurements provided.

## CONCLUSIONS

The primary goal of this work was to enhance the positioning precision of a robotic manipulator mounted on a mobile platform. Numerical methods, primarily FEM and kinematic simulations, were used during the design phase to predict and minimize the effects of segment deflections and joint positioning errors. The improved manipulator design, informed by these numerical analyses, significantly reduced expected displacements of the end-effector compared to the previous version—by more than five times in critical configurations (e.g., reducing total displacement from around 37 mm to below 7 mm). Subsequent experimental tests confirmed the effectiveness of the design improvements. The results, summarized in Table 8, show that the improved manipulator achieved positioning precision values ranging from approximately 2.95 mm ± 3.76 mm at point P4 up to 10.11 mm ± 4.99 mm at point P2. In contrast, the previous manipulator showed significantly higher positioning precision errors, ranging from about 14.28 mm ± 9.30 mm at point P4 to 21.40 mm ± 7.91 mm at point P3. These results indicate that the improved manipulator consistently outperforms the older design, reducing positioning errors by roughly a factor of 3 to 7 depending on the measurement point.

In conclusion, incorporating numerical analysis during the design process allowed identification and mitigation of key factors affecting positioning precision. This approach led to a marked improvement in manipulator accuracy and reliability, crucial for demanding applications on mobile robotic systems.

## Acknowledgments

The new manipulator project was funded by the Ministerstwo Nauki i Szkolnictwa Wyższego as part of the grant *Studenckie Koła Tworzą Innowacje*, edition 4.

## REFERENCES

- Schuster MJ, Brunner SG, Bussmann K, Büttner S, Dömel A, Hellerer M, Lehner H, Lehner P, Porges O, Reill J, Riedel S, Vayugundla M, Vordermayer B, Bodenmüller T, Brand C, Friedl W, Grixia I, Hirschmüller H, Kaßbecker M, Márton Z-C, Nissler C, Ruess F, Suppa M, Wedler A. Towards autonomous planetary exploration: The lightweight rover unit (LRU), its success in the SpaceBotCamp challenge, and beyond. *J. Intell. Robot. Syst.* 2019 Mar;93(3–4):461–494. <https://doi.org/10.1007/s10846-017-0680-9>
- Habibian S, Dadvar M, Peykari B, Hosseini A, Salehzadeh MH, Hosseini AHM, Najafi F. Design and Implementation of a Maxi-Sized Mobile Robot (Karo) for Rescue Missions. *Robomech J.* 2021 Jan;8:1. <https://doi.org/10.1186/s40648-020-00188-9>
- Ibna Rouf U, Ahmad N, Ghosh A, Jahin J, Rahman MM, Iqbal I, Islam MT, Farzana F, Rahman MM, Ehsan UR, Sharmin T. Design and Implementation of the Next Generation Mars Rover. In: *Proc. 21st Int. Conf. on Computer and Information Technology (ICCIT)*. Dhaka, Bangladesh; 2018 Dec. [https://www.researchgate.net/publication/330401821\\_Design\\_and\\_Implementation\\_of\\_the\\_Next\\_Generation\\_Mars\\_Rover](https://www.researchgate.net/publication/330401821_Design_and_Implementation_of_the_Next_Generation_Mars_Rover)
- Wu Z, Chen Y, Xu W. A light space manipulator

- with high load-to-weight ratio: System development and compliance control. *Sci. Robot.* 2021:9760520. <https://doi.org/10.34133/2021/9760520>
5. Chen W-H, Tsai Y-H, Lin C-Y. Development of a dual-joint harmonic drive actuator robotic arms system for compliant motion control. *Int. J. iRobotics.* 2024 Feb;7(2):1–10. <https://iroboticsjournal.org/index.php/irobotics/article/view/186>
  6. Yin J, Fan C, Zhang Y, Liu Y. A unified design for lightweight robotic arms based on unified description of structure and drive trains. *Int. J. Adv. Robot. Syst.* 2017 Jun;14(3):1729881417716383. <https://doi.org/10.1177/1729881417716383>
  7. Han L, Luo C, Cheng X, Xu W. Development of modular joints of a space manipulator with light weight and wireless communication. In: *Intelligent Robotics and Applications (ICIRA 2017), Lecture Notes in Computer Science.* Springer; 2017, 10464, 650–661. [https://doi.org/10.1007/978-3-319-65298-6\\_58](https://doi.org/10.1007/978-3-319-65298-6_58)
  8. Wang et al. Development of a Lightweight and High-efficiency Compact Cycloidal Reducer for Legged Robots 2019. [https://www.researchgate.net/publication/337518831\\_Development\\_of\\_a\\_Lightweight\\_and\\_High-efficiency\\_Compact\\_Cycloidal\\_Reducer\\_for\\_Legged\\_Robots](https://www.researchgate.net/publication/337518831_Development_of_a_Lightweight_and_High-efficiency_Compact_Cycloidal_Reducer_for_Legged_Robots)
  9. Semenchuk R. Investigation of the accuracy of the manipulator of the robotic complex constructed on the basis of cycloidal transmission. *Technology Audit and Production Reserves.* 2021;5(3):33–37. <https://doi.org/10.15587/2706-5448.2021.237326>
  10. Lv X, Yang Y, Zeng W, Xu D. Lightweight Design of Six-DOF Tandem Manipulator Based on Additive Manufacturing Technology. *IOP Conf. Ser.: Mater. Sci. Eng.* 2019;612(3):032145. <https://doi.org/10.1088/1757-899X/612/3/032145>
  11. Rui Y, Liu Y, Zhang Z, Tu Z, Wu J, Wei N, Zhao Z. Topology optimization design of the main structure of 6-DOF manipulator based on the variable density method. *Mech. Eng. Sci.* 2022;4(1):14–19. <https://doi.org/10.33142/mes.v4i1.7513>
  12. Cruz F, Safeea M, Babcsinchi M, Neto P. Design and 3D Printing Fabrication of a Low-Cost Lightweight Robot Manipulator. In: *Flexible Automation and Intelligent Manufacturing: The Human-Data-Technology Nexus (FAIM 2022), Lecture Notes in Mechanical Engineering,* 2023 Feb., 1143, 387–394. [https://doi.org/10.1007/978-3-031-17629-6\\_40](https://doi.org/10.1007/978-3-031-17629-6_40)
  13. Gutiérrez S, Zotović R, Navarro MD, Meseguer MD. Design and manufacturing of a prototype of a lightweight robot arm. *Procedia Manufacturing.* 2017 Jun;13:283–290. <https://doi.org/10.1016/j.promfg.2017.09.072>
  14. Huang X, Kong L, Dong G. Modeling and compensation of motion errors for 6-DOF robotic manipulators. *Appl. Sci.* 2021, Oct, 11(21):8–12. <https://doi.org/10.3390/app112110100>
  15. Sahu S, Choudhury B. Static analysis of a 6-axis industrial robot using finite element analysis. *Int. J. Mech. Eng. Technol.* 2017 Mar;8(3):49-55. <http://iaeme.com/Home/issue/IJMET?Volume=8&Issue=3>
  16. Jawale H, Thorat H. Positional error estimation in serial link manipulator under joint clearances and backlash. *Journal of Mechanisms and Robotics,* 2013 Jul;5(2):021003 <https://doi.org/10.1115/1.4023556>
  17. Deng S, Wang Y, Cai H, Li K, Yang F, Wang Y. Structural Topology Optimization Research for a Six-DOF Space Robotic Manipulator. *Adv. Eng. Res.* 2018 Mar;2018 Int. Conf. Mech. Elect. Control Autom. Eng. (MECAE 2018):543–548. <https://doi.org/10.2991/mecae-18.2018.88>
  18. Decker Ž, Tretjakovas J, Drozd K, Rudzinskas V, Walczak M, Kilikevičius A, Matijosius J, Boretska I. Material's strength analysis of the coupling node of axle of the truck trailer. *Materials.* 2023 Apr;16(9):3399. <https://doi.org/10.3390/ma16093399>
  19. International Organization for Standardization. *Manipulating Industrial Robots – Performance Criteria and Related Test Methods.* ISO 9283:1998. 2nd ed. Geneva: ISO; 1998.
  20. Kumičáková D, Tlach V, Cíсар M. Testing the Performance Characteristics of Manipulating Industrial Robots. *Transactions of the VŠB - Technical University of Ostrava, Mechanical Series.* 2016 Sep;62(1):39-50. <https://doi.org/10.22223/tr.2016-1/2009>
  21. Kuric I, Tlach V, Ságová Z, Cíсар M, Gritsuk I. Measurement of Industrial Robot Pose Repeatability. *MATEC Web Conf.* 2018 Feb;244:01015. <https://doi.org/10.1051/mateconf/201824401015>
  22. FANUC Robotics America, Inc. LR Mate 200iC Series & R-30iA Mate Controller – Datasheet. Rochester Hills, MI; 2009. Available from: [https://www.fanucamerica.com/cmsmedia/datasheets/LR%20Mate%20200iC%20Series\\_10.pdf](https://www.fanucamerica.com/cmsmedia/datasheets/LR%20Mate%20200iC%20Series_10.pdf)